INTERFACE FOCUS

royalsocietypublishing.org/journal/rsfs

Research

Cite this article: Anderson RP *et al*. 2020 Aluminosilicate haloes preserve complex life approximately 800 million years ago. *Interface Focus* **10**: 20200011.
http://dx.doi.org/10.1098/rsfs.2020.0011

Accepted: 21 April 2020

One contribution of 15 to a theme issue 'The origin and rise of complex life: integrating models, geochemical and palaeontological data'.

Subject Areas:
astrobiology

Keywords:
Proterozoic eon, early eukaryotes, clay minerals, complex life, metazoan antiquity, taphonomy

Author for correspondence:
Ross P. Anderson
e-mail: ross.anderson@all-souls.ox.ac.uk

Electronic supplementary material is available online at https://doi.org/10.6084/m9.figshare.c.4963142.

THE ROYAL SOCIETY PUBLISHING

Aluminosilicate haloes preserve complex life approximately 800 million years ago

Ross P. Anderson[1,2], Nicholas J. Tosca[2], Gianfelice Cinque[3], Mark D. Frogley[3], Ioannis Lekkas[3], Austin Akey[4], Gareth M. Hughes[5], Kristin D. Bergmann[6], Andrew H. Knoll[7] and Derek E. G. Briggs[8]

[1]All Souls College, University of Oxford, Oxford OX1 4AL, UK
[2]Department of Earth Sciences, University of Oxford, Oxford OX1 3AN, UK
[3]Diamond Light Source, Harwell Science and Innovation Campus, Didcot OX11 0DE, UK
[4]Center for Nanoscale Systems, Harvard University, Cambridge, MA 02138, USA
[5]Department of Materials, University of Oxford, Oxford OX1 3PH, UK
[6]Department of Earth, Atmospheric, and Planetary Sciences, Massachusetts Institute of Technology, Cambridge, MA 02139, USA
[7]Department of Organismic and Evolutionary Biology, Harvard University, Cambridge, MA 02138, USA
[8]Department of Geology and Geophysics, Yale University, New Haven, CT 06511, USA

RPA, 0000-0002-0558-7563; NJT, 0000-0003-4415-4231; AHK, 0000-0003-1308-8585; DEGB, 0000-0003-0649-6417

Mudstone-hosted microfossils are a major component of the Proterozoic fossil record, particularly dominating the record of early eukaryotic life. Early organisms possessed no biomineralized parts to resist decay and controls on their fossilization in mudstones are poorly understood. Consequently, the Proterozoic fossil record is compromised—we do not know whether changing temporal/spatial patterns of microfossil occurrences reflect evolution or the distribution of favourable fossilization conditions. We investigated fossilization within the approximately 1000 Ma Lakhanda Group (Russia) and the approximately 800 Ma Svanbergfjellet and Wynniatt formations (Svalbard and Arctic Canada). Vertical sections of microfossils and surrounding matrices were extracted from thin sections by focused ion beam milling. Elemental mapping and synchrotron-based infrared microspectroscopy revealed that microfossils are surrounded by haloes rich in aluminium, probably hosted in kaolinite. Kaolinite has been implicated in Cambrian Burgess Shale-type (BST) fossilization and is known to slow the growth of degraders. The Neoproterozoic mudstone microfossil record may be biased to tropical settings conducive to kaolinite formation. These deposits lack metazoan fossils even though they share fossilization conditions with younger BST deposits that are capable of preserving non-mineralizing metazoans. Thus metazoans, at least those typically preserved in BST deposits, were probably absent from sedimentary environments before approximately 800 Ma.

1. Introduction

Due to a lack of organisms with readily fossilized hard parts, it has long been observed that the pre-Cambrian fossil record is impoverished compared with its Phanerozoic counterpart [1]. However, over the last approximately 70 years palaeontologists have discovered a number of exceptionally preserved assemblages of diverse microfossils in Proterozoic rocks [2,3]. Three principal lithologies record microfossils: early diagenetic cherts and phosphates, and mudstones [4]. Evidence from the record of eukaryotic microfossils suggests that the mudstone record dominates—47 of 59 fossiliferous assemblages in a recent compilation are mudstone hosted [4]. We know little of the taphonomic processes that operated in mudstones [5]. What factors promoted fossilization? What determines which mudstones preserve non-biomineralized microfossils? Understanding taphonomy in Proterozoic mudstones is vital to our efforts to chart Proterozoic evolution. Furthermore, we need to understand whether there

Table 1. Interpreted phylogenetic affinities and associated biopolymers of the studied microfossils: Lakhanda [24,25], Svanbergfjellet [2,26–28] and Wynniatt [29]. Biopolymers taken from [30–34].

	phylogenetic affinity	principal biopolymer	thin section, university collection, England Finder coordinates
Lakhanda			
Siphonophycus	?cyanobacterium	sheaths of carbohydrate fibrils	LK67, Cambridge, UK, N32/2
Svanbergfjellet			
Proterocladus major	chlorophyte	carbohydrates including cellulose	86-G-62–52, Harvard, MA, N47/2
Germinosphaera fibrilla	?eukaryote (possible vaucheriacean alga or fungus)	likely aliphatic composition similar to sporopollenin or algaenan	86-G-62–68, Harvard, MA, Q48/4
microfossil fragment	?eukaryote	undetermined	86-G-62-54, Harvard, MA, L26/2
Wynniatt			
?*Ostiana* (or possibly *Palaeastrum*)	?cyanobacterium (or chlorophyte)	lipids and proteins with possible sheaths of carbohydrate fibrils (or, in the case of chlorophyte, carbohydrates including cellulose)	88-KL-131-2, Cambridge, UK, D35/2
Siphonophycus	?cyanobacterium	sheaths of carbohydrate fibrils	88-KL-131-2, Cambridge, UK, Q46/2

are temporal or spatial biases to the Proterozoic microfossil record. Patterns of microfossil diversity may represent real ecological patterns, but they could also represent spatial/temporal changes in the availability of environmental conditions conducive to fossilization. Our inability to unravel these scenarios fundamentally compromises the use of mudstone-hosted microfossils to reveal Proterozoic evolutionary history.

Examples of soft tissue fossilization [6] in Phanerozoic mudstones provide a basis for taphonomic hypotheses that can be tested on Proterozoic deposits. Cambrian Burgess Shale-type (BST) deposits are the most studied, preserving early metazoans including diverse organisms that lacked mineralized skeletons [7]. A variety of factors have been proposed to influence BST fossilization, including oxidant supply, sediment composition, the propensity of soft tissues for replication in authigenic minerals (e.g. pyrite, phosphate and clay minerals) and cementation of the overlying sediment (see [8] for a review). A role for clay minerals has been posited more recently: experiments have shown that the aluminium- and iron-rich clays kaolinite and berthierine, which are major constituents of a large proportion of Cambrian strata hosting BST fossils [9,10], slow the growth of decay bacteria [11] and increase decay resistance through clay–organic matter interactions [12–18]. Evidence is also emerging that kaolinite, in particular, may attach to or precipitate on some tissues early in diagenesis, helping to conserve them by providing a protective coating and/or facilitating polymerization [14,19,20]. Intriguingly, elements indicative of these clays (e.g. aluminium and iron) have also been reported adjacent to some Proterozoic fossils, but their host phases are difficult to constrain [21–23]. Do aluminium- and/or iron-rich clay minerals promote fossilization in Proterozoic strata? Do they promote fossilization not only of metazoans but also of other phylogenetic groups such as eukaryotic algae, or even cyanobacteria, which have diverse biopolymer compositions?

We investigated the taphonomy of microfossils (both probable eukaryotes and cyanobacteria; table 1) from three exceptional Tonian (1000–717 Ma) deposits: the approximately 1000 Ma Lakhanda Group (Russia) [24,25], and the approximately 800 Ma Svanbergfjellet (Svalbard) [26] and Wynniatt (Canada) formations [29]. These assemblages include some of the best preserved and most diverse pre-Ediacaran fossils and often include microfossils that are more fragile than the decay-resistant spheroidal acritarchs commonly recovered from Proterozoic strata [2,4]. More fragile forms include relatively large (up to millimetre scale) multicellular morphologies and those that possess intricate spines or processes [7,24–26,29]. For example, microfossils from the Svanbergfjellet Formation may represent some of the oldest examples of multicellular eukaryotic green algae (chlorophytes) [26,27]. We used a novel combination of microanalytical techniques to probe sediment mineralogy immediately adjacent to microfossil cell walls. These data illuminate the role of clay minerals in Proterozoic taphonomy, allowing comparisons with BST fossilization.

2. Material and methods

Microfossils were identified in thin sections cut sub-parallel to sedimentary laminae that were obtained for previous studies (as in BST fossilization [7], fossils are compressed into two dimensions parallel to laminae). Thin section number, university collection and England Finder coordinates are given in table 1 for each microfossil/population studied. Thin sections from Harvard University, Cambridge, MA, are deposited in the Paleobotanical Collections of the Harvard University Herbaria, while the sections from the University of Cambridge, Cambridge, UK, are in the collections of N. Butterfield. A filamentous microfossil (sheathed cyanobacterium), *Siphonophycus*, was examined from the Lakhanda Group, whereas three microfossils were analysed from the Svanbergfjellet Formation: the chlorophyte *Proterocladus major*, the acanthomorphic acritarch (eukaryote) *Germinosphaera fibrilla* and an unidentified fragment of a larger microfossil (eukaryote). A monostromatic population of spheroids, possibly *Ostiana* (cyanobacterium) or the chlorophyte *Palaeastrum* (we refer to this population as *Ostiana*), and another *Siphonophycus* specimen were analysed from the Wynniatt Formation. For details on phylogenetic assignments, see table 1. The microfossils from each deposit were derived from single rock samples, one per deposit (Lakhanda, LK67, Cambridge, UK; Svanbergfjellet, 86-G-62,

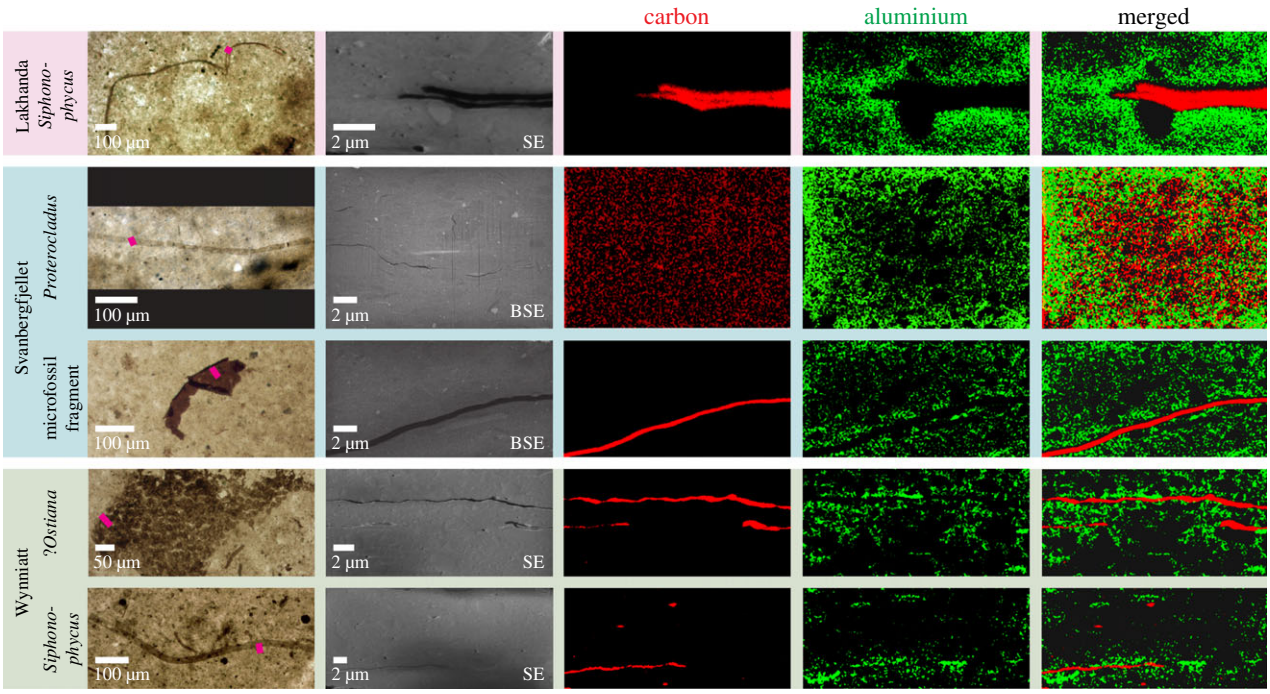

Figure 1. Studied microfossils with elemental distributions. Light photomicrographs of microfossils in thin section. Locations of extracted vertical sections shown by pink bars. SEM micrographs of extracted vertical sections and EDS maps showing carbon and aluminium distributions. Carbon constitutes the microfossils which are surrounded by a concentration of aluminium. Secondary electron (SE) or backscatter electron (BSE) SEM images were used to minimize charging effects. Specimen details are listed in table 1. SEM and EDS operating conditions for each map/image are listed in electronic supplementary material, table S1. Light and SEM images of the Svanbergfjellet *Germinosphaera* specimen/vertical section are given in electronic supplementary material, figure S1.

Harvard, MA; Wynniatt, 88-KL-131, Cambridge, UK). Vertical sections (approx. 30 µm × 10 µm × 1 µm) of microfossils and adjoining matrices were extracted perpendicular (or sub-perpendicular) to sedimentary laminae from the thin sections using focused ion beam (FIB) milling at the Harvard Center for Nanoscale Systems (CNS), Cambridge, MA, and attached to copper transmission electron microscopy (TEM) grids. Milling was performed on an FEI Helios 660 Dual-Beam FIB/SEM (scanning electron microscope) equipped with an Autoprobe 400 micromanipulator.

Vertical sections were imaged using the SEM on the FEI Helios 660 at CNS and also on a Carl Zeiss Merlin SEM equipped with an Oxford Instruments X-Max^N 150 mm^2 X-ray detector at the Department of Materials, University of Oxford (ODM), Oxford, UK. Energy dispersive X-ray spectroscopy (EDS) at ODM was used to map elemental distributions across vertical sections for all samples except *Germinosphaera* (which was destroyed in sample manipulation before maps could be generated). In order to reduce sampling volume (thereby increasing spatial resolution) and reduce charging effects, EDS was carried out at voltages below 10 kV, with higher energy analysis to confirm the identity of elements when required (see electronic supplementary material, table S1 for configurations). Maps were processed using AZtec v3.3 and the TruMap function. Synchrotron-based Fourier transform infrared (FTIR) microspectroscopy at the MIRIAM beamline of Diamond Light Source, Didcot, UK, was used to identify the mineral hosts of elemental variations in all vertical sections. The beamline was coupled to a Bruker Vertex 80 V FTIR spectrometer and Hyperion 3000 microscope equipped with a 50 µm, LN_2 cooled, midband mercury–cadmium–telluride detector. About 256 scans were coded at 4 cm^{-1} spectral resolution per point. The infrared focal spot was confined to a diffraction limited area using slits of effective aperture 3 × 3 µm at the sample, via × 36 optics in transmission geometry with numerical aperture (NA) = 0.5. The sample was mapped across this aperture with step size 1 µm, oversampling with respect to the aperture size. In these conditions, the resulting spatial resolution is expected to be diffraction limited and wavelength (λ) dependent, approximately at the Abbe resolution limit = λ/2NA = λ (at NA 0.5). The spatial resolution is about 2.8 µm for the M–OH spectral region of interest.

Finally, powder X-ray diffraction (XRD) was performed on each rock sample using a PANalytical Empyrean diffractometer at the Department of Earth Sciences, University of Oxford, Oxford, UK, employing a Co Kα source and a PIXcel-1D detector. A substitute for the Svanbergfjellet sample, from the same locality/stratigraphic horizon, was obtained from the Cambridge, UK, collections (sample 99-L-15) as no 86-G-62 material remains. Mineral identifications were confirmed using the International Centre for Diffraction Data (ICDD) Powder Diffraction File-4+ database (http://www.icdd.com/products/pdf4.htm) and the reference intensity ratio method [35]. Clay mineral species were distinguished by weak but diagnostic peaks commonly manifested as a composite reflection from 060 and/or 33-1 [36].

3. Results

SEM imaging of the vertical sections revealed the cross-sectional structure of the microfossils (figure 1), which varies in thickness. The Svanbergfjellet microfossil *Proterocladus* is only tens of nanometres thick and hardly perceptible, while the Lakhanda *Siphonophycus* specimen and both the *Germinosphaera* specimen and the unidentified microfossil fragment from Svanbergfjellet are up to approximately 0.5 µm thick. All specimens from the Wynniatt Formation are intermediate in thickness (approx. 0.2–0.4 µm). In some cases, microfossil walls have split and infilled with matrix, as in some of the Wynniatt *Ostiana* individuals, but the majority are intact. The Wynniatt *Ostiana* cluster is evident on two sedimentary laminae in the sample and thus may represent multiple colonies or one colony that has been infiltrated by sediment during deposition

(figure 1). The *Siphonophycus* specimen from Lakhanda may be split into two or represents two superimposed filaments (figure 1). SEM images confirmed that microfossils are compressed sub-parallel to sedimentary laminae. The lithologies of the samples are similar, with most sediment grains ≪1 µm and only sparse grains approximately 1 µm, around which microfossils may be deflected: e.g. the vertical section of the Lakhanda *Siphonophycus* (figure 1). Larger grains are normally rounded, although some oblong sub-angular grains, which can reach greater than 5 µm in maximum dimension (figure 1) with long axes parallel to sedimentary laminae, are associated with the Svanbergfjellet microfossils.

EDS analysis revealed that the microfossils are composed of carbon (figure 1), although the result was ambiguous for the Svanbergfjellet *Proterocladus* specimen, probably reflecting its very thin cross-section and the relatively large volume producing X-rays which, even at 5–10 kV, can have a masking effect on local elemental enrichments. The Lakhanda *Siphonophycus* specimen and the Wynniatt *Ostiana* specimens are enriched in sulfur. The sediment surrounding all the microfossils is largely similar (see electronic supplementary material, figure S2), dominated by silicon and oxygen with minor aluminium, carbon, chlorine, iron, magnesium, nitrogen, phosphorus, potassium, sodium and sulfur, reflecting a siliciclastic matrix with contributions from both organic matter and diagenetic minerals. Calcium is also present but sparsely distributed, probably reflecting a minor admixture of carbonate minerals. Larger rounded quartz grains are present (identified by a dominantly silicon and oxygen composition). Larger sub-angular grains in Svanbergfjellet vertical sections are enriched in magnesium and iron, indicative of chlorite.

Aluminium is generally enriched adjacent to microfossil carbon compared with the matrix, often forming a halo (figure 1). Aluminium haloes with a thickness less than 3 µm are particularly apparent surrounding the Svanbergfjellet unidentified microfossil fragment and the Lakhanda *Siphonophycus* specimen. None of the Wynniatt vertical sections shows a contiguous halo, but there are discontinuous aluminium enrichments adjacent to microfossils. The only vertical section for which aluminium enrichments adjacent to microfossils were not identified unambiguously is that of the Svanbergfjellet *Proterocladus* specimen; however, as noted regarding its carbon composition, this may be due to its thin cross-section and EDS masking effects.

SEM imaging provides evidence that the aluminium enrichments occur in platy materials, presumably clays. SEM of the Wynniatt *Siphonophycus* vertical section shows a halo of platy material, parallel to sedimentary laminae, extending less than 0.5 µm around the microfossil (figure 2). A layer of matrix characterized by a lack of the larger grains or pseudo-hexagonal crystals that are common elsewhere (possibly muscovite) extends less than 1 µm beyond this layer. Coarser crystals often display planar interlocking boundaries, suggesting a phase of overgrowth after physical deposition. These observations indicate differential chemistry and mineralogy adjacent to the microfossil compared with that of the matrix. The finely crystalline and platy nature of the material hosting the aluminium enrichments identified by EDS suggests that aluminium may be bound largely in a clay mineral structure.

Synchrotron-based FTIR microspectroscopy confirmed that the most likely clay mineral host of these aluminium enrichments is kaolinite and its metamorphic products.

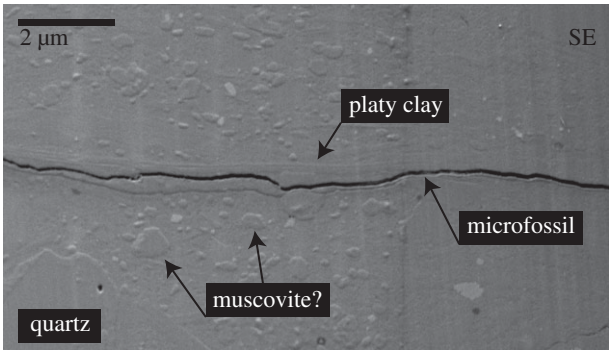

Figure 2. SEM secondary electron (SE) micrograph of the vertical section of *Siphonophycus* from the Wynniatt Formation. Microfossil cross-section is surrounded by a halo of a platy mineral likely to be kaolinite. Coarser crystals with planar interlocking boundaries (likely to be muscovite) and large quartz grains are also highlighted. SEM operating conditions are listed in electronic supplementary material, table S1.

Kaolinite can be identified using FTIR by a series of three M–OH bands at approximately 3620, approximately 3652 and approximately 3694 cm^{-1} [37]. For randomly oriented powders, the approximately 3620 and approximately 3694 cm^{-1} bands are more intense than the approximately 3652 cm^{-1} band; their frequencies are also sufficiently distinct from illite-group and chlorite-group minerals to allow unambiguous identification of kaolinite. FTIR microspectra from all Lakhanda and Svanbergfjellet vertical sections clearly differentiated these bands (figure 3). Vertical sections of the Wynniatt Formation microfossils showed a broad M–OH band between approximately 3500 and approximately 3700 cm^{-1}, with no observable kaolinite bands (figure 3). This probably reflects a dominance of illite/muscovite in Wynniatt clay mineralogy [37]. Any kaolinite, if present, is diluted beyond the detection limit in FTIR microspectra. Mild contact metamorphism of Wynniatt strata [38] may have transformed kaolinite to illite/muscovite [39]. Microfossil carbon is not recorded in our FTIR microspectra. Other Proterozoic microfossils are known to produce FTIR spectra indicative of their carbon composition [40]. Its absence in our analysis probably reflects a drowning of any organic signature given the limited amount of microfossil material compared with the mineral matrix.

The total area under each band provides a proxy for the distribution of minerals. When mapped across the vertical sections, the areas under the approximately 3694 cm^{-1} band and the entire M–OH region show some variations between specimens (figure 4) but cannot be fully matched to the EDS maps (figure 1; electronic supplementary material, figure S2). In the Lakhanda *Siphonophycus* and Svanbergfjellet vertical sections, both FTIR bands are weaker on and around the microfossils, a contrast that is especially evident near hotspots (red) where the bands are locally strong. This is indicative of a lack of OH within microfossils at the approximately 2.8 µm resolution of the FTIR map, rather than a lack of OH groups around microfossils. In the Lakhanda *Siphonophycus* vertical section, the region where OH bands are weaker extends down vertically, perhaps corresponding to the larger quartz grain below the microfossil (electronic supplementary material, figure S2). The source of the FTIR band hotspots is not evident in light microscopy or EDS images (figure 1; electronic supplementary material, figure S2), but overall we can conclude that kaolinite is present across the bulk of the mineral phase of the four FTIR maps of the vertical sections

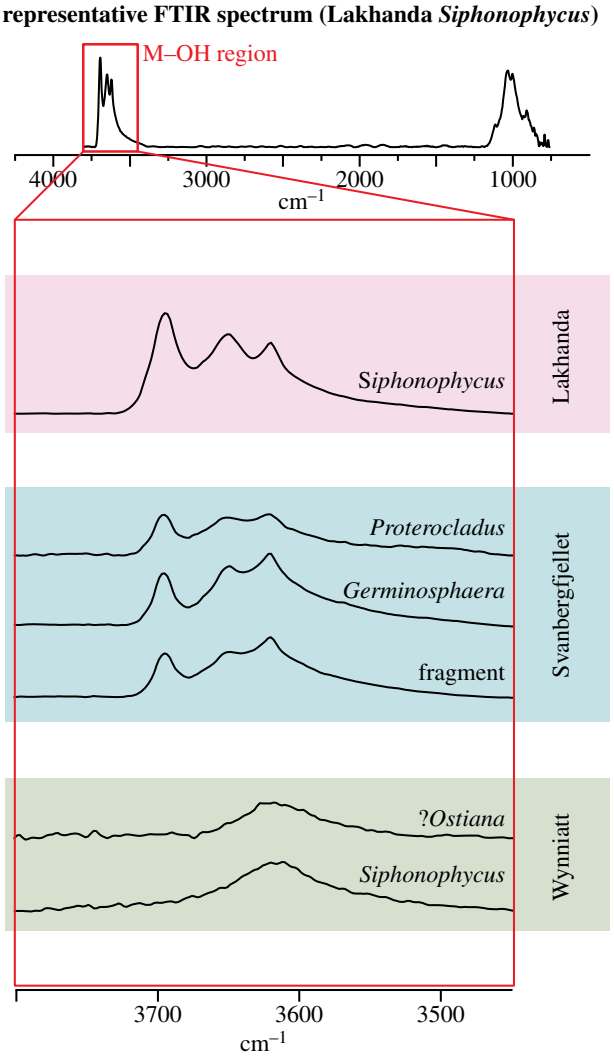

Figure 3. Representative synchrotron-based FTIR microspectra. Top: Representative total spectrum showing an average of Lakhanda *Siphonophycus* spectra: numbers 188, 189, 190, 203, 204, 205, 218, 219, 220. Both M–OH bands are present plus a broad silicate peak at approximately 1000 cm^{-1} which is not resolved in sufficient detail to interpret its mineralogical components. Below are representative spectra from the M–OH region for each vertical section plotted on the same vertical scale. Characteristic bands at approximately 3620, approximately 3652 and approximately 3694 cm^{-1} are recorded for the vertical sections from Lakhanda and Svanbergfjellet, while a single broad band between approximately 3500 and approximately 3700 cm^{-1} is recorded for the vertical sections from Wynniatt. Representative spectra: Lakhanda *Siphonophycus* number 237; Svanbergfjellet *Proterocladus* number 150, *Germinosphaera* number 150 and microfossil fragment number 263; and Wynniatt *Ostiana* number 240 and *Siphonophycus* number 204. See electronic supplementary material, table S2 for FTIR data.

in figure 4. The large black region on the left side of the Lakhanda *Siphonophycus* FTIR maps is where the band strength is high and saturated with respect to the colour scale in the image (greater than 4.6 or greater than 13 for the 3694 cm^{-1} and full M–OH band, respectively). This apparent increase in band strength may include optical effects of the interaction between the infrared beam and the metallic weld close (less than 5 µm) to the attachment of the sample to the TEM grid. The ratio of the approximately 3694 cm^{-1} band to the entire M–OH region reflects the distribution of kaolinite with respect to total illite [37]. At the approximately 2.8 µm spatial resolution available, a fairly constant abundance of kaolinite, with respect to total illite, across each vertical section is implied by the similar ratios, with no clear correspondence to the microfossils. The black zig-zag patterns along the edges of the vertical section are artefacts resulting from optical scattering from the vertical section. These biomineralogical data from synchrotron-based FTIR microspectroscopy confirm that kaolinite and/or its metamorphic products are present in all vertical sections. Although the FTIR maps do not fully resolve the distribution of minerals with the necessary spatial resolution, in concert with EDS maps they provide a compelling case for kaolinite enrichment adjacent to microfossils.

Further confirmation that kaolinite represents a component of the fossiliferous rocks is evident in bulk powder XRD analyses of hand samples from each locality (table 2), although these do not sample individual laminae. All samples are dominated by muscovite (34–74%, mean = 57.7, s.d. = 21, n=3) and quartz (26–58%, mean = 37, s.d. = 18.2, n = 3); the Svanbergfjellet sample contains minor chlorite (7%) in addition. The reference intensity ratio method detected kaolinite (8%) only in the Lakhanda sample. However, weak but diagnostic peaks manifested as a composite reflection from 060 and/or 33-1 showed that kaolinite is also present in the Svanbergfjellet sample. Relative abundance of clay species can be obtained as a linear function of the area underlying these peaks [36]. This method shows that kaolinite represents 30.7% of total clay (glauconite + illite type 1 + illite type 2 + kaolinite) in the Svanbergfjellet sample and 66.2% in the Lakhanda sample. The high kaolinite content of the Lakhanda sample is consistent with mineralogical studies of these strata [41]. The absence of kaolinite from powder XRD and the high illite content (90%) of the Wynniatt sample is consistent with the broad M–OH band in the FTIR data, perhaps reflecting complete transformation of any precursor kaolinite to illite/muscovite during contact metamorphism [38]. 060 and/or 33-1 composite reflections suggest that glauconite (10%) is also present in the Wynniatt sample.

4. Discussion

4.1. Kaolinite and Proterozoic fossilization

The identification of aluminium haloes surrounding microfossils, hosted in kaolinite and its metamorphic products illite/muscovite, prompts comparisons with Cambrian BST fossilization. Strata with BST fossilization globally are enriched in berthierine (a diagenetic product of kaolinite when iron is present) [9,10]. Recently, it has also been observed that metazoan fossils from the Burgess Shale at the Walcott Quarry (Canada) are themselves enriched in kaolinite compared with their surrounding mudstone matrix [19,20]. The kaolinite enrichment on Burgess Shale fossils is attributed to bonding between the fossil organic matter and the mineral during organism decay, which is inferred to have slowed or arrested subsequent transformation of fossil-associated kaolinite to other minerals during greenschist facies metamorphism [20,42]. This interpretation implies that local decreases in pH induced by decay [43] result in positively charged carcase organic matter, facilitating bonding with negatively charged edge sites on kaolinite [e.g. 44–46]. These edge sites, which account for 10–20% of the surface area of the mineral [45], are known to be relatively acidic, increasing the likelihood that they would persist in a negatively charged state at relatively low pH, maximizing the probability of

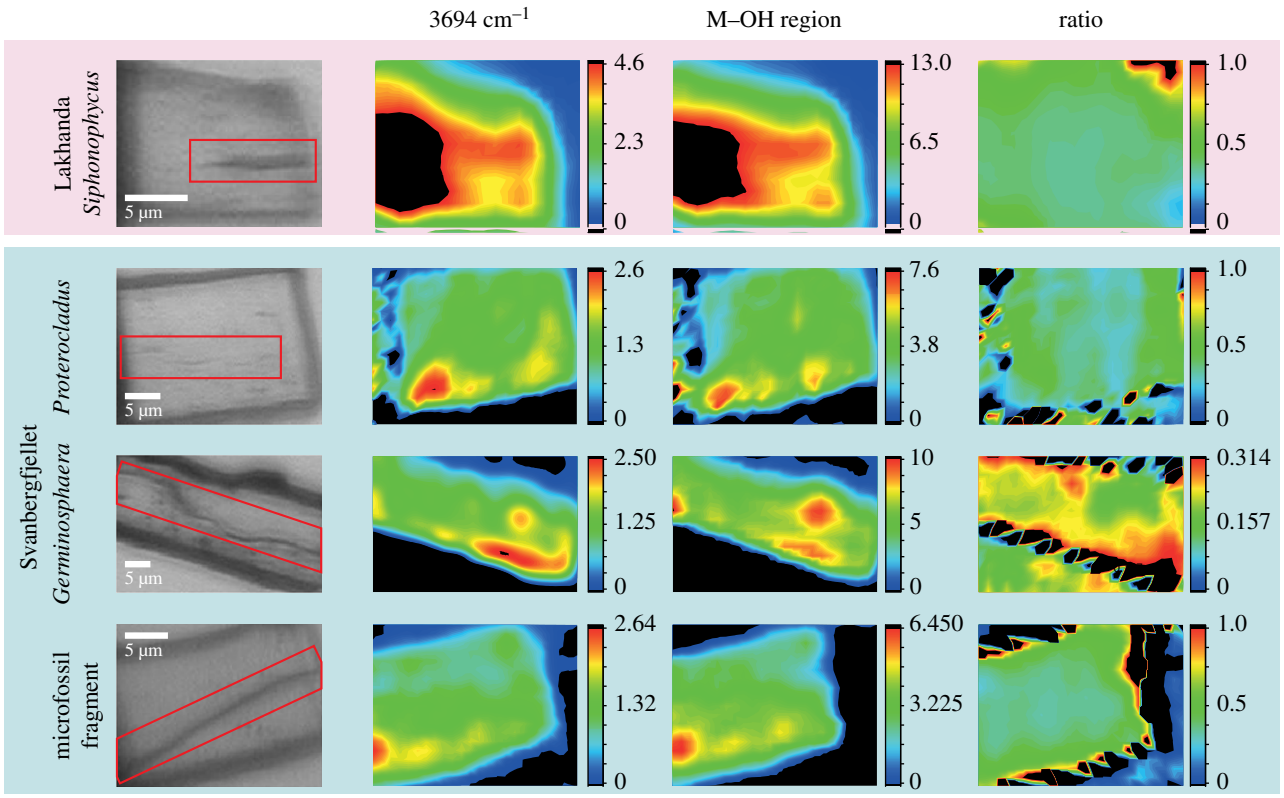

Figure 4. Synchrotron-based FTIR microspectroscopy maps of compositional variation indicated by the areas below the approximately 3694 cm^{-1} band, the entire M–OH region (integrated band intensities in arbitrary units), and the ratio of these two areas, for Lakhanda and Svanbergfjellet vertical sections which show clearly defined M–OH bands. The light microscopy images of vertical sections (left) indicate the position of the microfossils (red boxes). See text for further details.

Table 2. Bulk powder XRD results. Percentage of each rock sample composed of different minerals is calculated by the reference intensity ratio method [35]. Clay speciation is also presented as a percentage of total clay (glauconite + illite 1 + illite 2 + kaolinite) using the relative areas of weak but diagnostic peaks from 060/33-1 [36]. Qtz = quartz, Musc = muscovite, Chl = chlorite, Kaol = kaolinite, Gl = glauconite, and Il1 and Il2 = two varieties of illite. Lakhanda sample LK67, Svanbergfjellet sample 99-L-15, and Wynniatt sample 88-KL-131.

	reference intensity ratio %				060/33-1 % total clay			
	Qtz	Musc	Chl	Kaol	Gl	Il1	Il2	Kaol
Lakhanda	58	34	0	8	0	0	33.8	66.2
Svanbergfjellet	27	65	7	0	0	6.6	62.6	30.7
Wynniatt	26	74	0	0	10	90	0	0

binding to organic matter [47,48]. It is unclear whether kaolinite attached to fossil organic matter was from the sediment, or whether it precipitated *in situ*. It has been argued that the chemical properties of kaolinite were a significant factor in the fossilization of Burgess Shale metazoans [19,20]. Kaolinite is known to promote polymerization and adsorption of a variety of organic molecules [44,45,49] and to trigger kerogen maturation upon pyrolysis [50]. It can stabilize pre-existing organic cross-links via the donation of electrons, reducing double bonds [51], as well as inhibit the growth of bacteria that promote decay [11]. Experimental studies have shown that kaolinite–organic interactions often promote the conservation of morphology in decaying metazoan tissues [12–18].

The aluminosilicate haloes surrounding the microfossils studied here suggest that kaolinite attachment and/or *in situ* precipitation onto microbial cell walls or enclosing sheaths, via a similar process to BST fossilization, was a significant factor in the preservation of microfossils in Proterozoic mudstones. These data add to recent studies that report concentrations of elements indicative of clays (e.g. aluminium and iron) adjacent to other Proterozoic fossils [21–23]. The organisms studied here probably represent a variety of evolutionary clades, including eukaryotic chlorophyte algae and cyanobacteria [24–27,29]. The cell walls and extracellular sheaths of these organisms were composed of different biomolecules (table 1) from those of the metazoans preserved in BST deposits, with variable resistance to decay [30,31]. Cyanobacteria cells are commonly enclosed by sheaths composed of chemically distinct carbohydrate fibrils which are relatively resistant to decay [32]—in the case of *Siphonophycus*, for example. *Ostiana*, on the other hand, may not possess a sheath; the cell walls probably comprised lipids and proteins [33]. Chlorophytes are dominated by carbohydrates, including cellulose, which make up the cell walls. In addition, acanthomorphic acritarchs, such as *Germinosphaera*, are commonly characterized by highly resistant walls of aliphatic composition

similar to sporopollenin or algaenan [34]. By contrast, metazoans, like those represented in BST deposits, are composed of a range of biomolecules including proteins, carbohydrates and lipids, although sclerotized and cuticularized tissues are preferentially preserved [52]. The similarity of kaolinite enrichments in fossils representing these different clades suggests that this type of fossilization is not biopolymer specific. Nor is it morphology dependent—the fossils studied here range in morphology from filaments and spheroids to multicellular remains and, in the case of Burgess Shale fossils, macroscopic forms. Indeed, numerous studies have already shown that clay minerals commonly attach to the organics of microbial organisms such as cyanobacteria in natural and experimental systems [53–58]. The enrichments of kaolinite adjacent to microfossil cell walls argue not only for a role for kaolinite in fossilization but, through organism–mineral interactions, a role for incipient microfossils in facilitating kaolinite enrichment in the first place. A similar process has also been used as an explanation for silica enrichments surrounding microfossils [59].

4.2. Biases of the Proterozoic shale-hosted microfossil record

Identifying a taphonomic role for kaolinite in Proterozoic mudstones, the dominant lithology for early microfossils [4], indicates that the Proterozoic mudstone-hosted fossil record may be biased to environmental settings that were rich in kaolinite or hosted conditions conducive to its formation, giving us pause for thought when considering temporal/spatial patterns in the Proterozoic microfossil record. Kaolinite today is primarily sourced from tropical weathering regimes where drainage is high and soil pH low [39]. Palaeogeographic reconstructions suggest that each of the studied deposits (Lakhanda Group—Siberia, Svanbergfjellet Formation—East Svalbard and Wynniatt Formation—Laurentia) formed in tropical to mid-palaeolatitudes [60], consistent with this interpretation. Moreover, reconstruction of seawater pH through geological time suggests that Neoproterozoic oceans were characterized by lower pH than their modern counterparts [61]. Such a palaeoenvironmental bias to fossilization is likely to be more acute for organisms where preservation of delicate morphology is required. The three assemblages studied include rarely preserved morphologies that were presumably more fragile (e.g. multi-celled, slender spines/processes) than those from other Proterozoic localities with microfossils [24–26,29]. It is not clear from our work whether the presence of kaolinite in the local environment is sufficient or kaolinite is required at a specific concentration.

4.3. Implications for our understanding of the antiquity of metazoans

Our results have specific implications for understanding the emergence of metazoan life. There is a disconnect between molecular clock estimates for the antiquity of metazoans and their earliest body fossils. A recent molecular analysis placed the last common ancestor of extant metazoans at 833–650 Ma [62], yet unambiguous body fossil evidence extends only as far as approximately 580 Ma (for example [63]). Where are the missing pre-580 Ma metazoan fossils? Can the gap be explained by taphonomic bias [64]? BST fossilization provides an unusually comprehensive picture of Cambrian metazoan diversity [62,65–67]; even microscopic metazoans are represented [68,69]. The demonstration that some Neoproterozoic mudstones share taphonomic pathways with BST deposits identifies at least three Tonian targets for early metazoan fossils. However, the microfossils in these assemblages represent microbial eukaryotes and bacteria [2,24–29,70,71]. Some large morphologically complex microfossils in Ediacaran mudstones have been interpreted as egg and/or diapause cysts of metazoans [72] and a similar interpretation has been advanced for a population of Tonian microfossils [73], but other interpretations have been proposed [74]. Macroscopic fossils, e.g. *Chuaria* and *Tawuia*, occur in two of the deposits (Svanbergfjellet and Wynniatt) [24–26,29], and although recent evidence suggests that some of these may be multicellular there is no evidence that they represent metazoans [75]. The lack of metazoan fossils in these deposits despite BST conditions conducive to their fossilization may indicate that metazoans had not evolved by approximately 800 Ma. If so, this provides a soft maximum age (a maximum age based on the probability that fossils of this age are not metazoans) for their appearance, as suggested previously [68] and employed in some molecular clocks [65] but without consideration of taphonomy. It could be argued that, even though metazoans are not a component of the three assemblages that we investigated, they could be present in others of similar age, or that small early metazoans are not preserved even by BST fossilization. Nonetheless this soft maximum age can now be applied with greater confidence.

4.4. Clay mineral–organic interactions and the search for fossils on Mars

Our results may also be relevant to the search for fossilized life on Mars [76]. A variety of clay minerals have been identified on Mars on the basis of orbital infrared spectroscopy, including illite, kaolinite, smectites, chlorites and serpentine minerals [77–79]. Clay minerals have been identified in crustal rocks that may encompass a wide range of palaeoenvironmental conditions. These deposits have been variably interpreted as *in situ* weathering profiles, fine-grained clastic sediments and hydrothermally altered crust [77–79]. Our data suggest that specific interactions between kaolinite mineral surfaces and solution may have facilitated the polymerization of organic molecules—a key step in promoting fossilization. These reactions, however, are dependent on the pH of the solution relative to the acidity of clay edge sites. It is reasonable to assume that these same principles apply to the early Martian surface; in suitable chemical conditions, kaolinite may have served a similar taphonomic role to that envisaged for samples described here. However, available data indicate that clay-rich deposits on early Mars experienced a much broader range in pore/bottom water pH, variable contact times with liquid water and large fluctuations in ionic strength [79,80]. Thus, taphonomically favourable clay mineral assemblages on Mars are best diagnosed in light of depositional and diagenetic constraints on fluid chemistry and a mechanistic consideration of clay mineral–organic interactions.

5. Conclusion

An understanding of taphonomy is critical to the interpretation of morphology and the environmental/temporal ranges of fossil taxa, and is particularly important for Proterozoic

palaeobiology where biomineralized tissues are absent. Kaolinite or its metamorphic equivalents are associated with all microfossils in the three Tonian deposits we studied, despite their phylogenetic, compositional and stratigraphic diversity. Our search for new microfossils, particularly fragile metazoans, in Proterozoic strata should focus on sites where kaolinite is likely to be present. These search criteria may also be valid when exploring other planets, such as Mars [76], for evidence of past life. Further studies should expand this investigation to a wider variety of Proterozoic fossiliferous mudstones, such as those of the Ediacaran Doushantuo Formation which do not contain complex metazoans [81], in order to determine the prevalence of appropriate taphonomic conditions across time and palaeoenvironments.

Data accessibility. Synchrotron-based Fourier transform infrared microspectroscopy data collected at the Diamond Light Source, Didcot, UK, and used to build figure 4 are available in the electronic supplementary material.

Authors' contributions. R.P.A., N.J.T., K.D.B. and D.E.G.B. designed the research. A.H.K. provided fossils. A.A. prepared vertical sections. R.P.A. and G.M.H. analysed vertical sections using SEM and EDS. R.P.A., G.C., M.D.F. and I.L. analysed vertical sections using synchrotron-based FTIR microspectroscopy. R.P.A. and N.J.T. analysed fossiliferous rocks using XRD. R.P.A. wrote the manuscript with discussion and input from all authors.

Competing interests. We declare we have no competing interests.

Funding. This work was supported by All Souls College, Diamond Light Source (SM15975-1 and SM21059-1), Geological Society of America, Geological Society of London, NASA Astrobiology Institute (NNA13AA90A), Yale Institute for Biospheric Studies and Yale Peabody Museum of Natural History. R.P.A. was supported by All Souls College and NASA (NNX14AP10H). This work was performed in part at the Center for Nanoscale Systems (CNS), a member of the National Nanotechnology Coordinated Infrastructure Network (NNCI), which is supported by the National Science Foundation under NSF award no. 1541959. CNS is part of Harvard University.

Acknowledgements. We are grateful to N. Butterfield for access to fossils, valuable discussion and comments on a draft of this paper. R.P.A. thanks the organizers of the Royal Society Discussion Meeting for the invitation to present at the meeting, in addition to P. Donoghue for valuable discussion and H. Bechtel, E. Clark, K. Clayton, B. Johnson, W. Samela and R. Tostevin for assistance with sample preparation and data collection. Diamond Light Source is acknowledged for beamtime SM15975-1 and SM21059-1 at MIRIAM beamline B22. Two anonymous reviewers provided constructive comments.

References

1. Knoll AH. 2003 *Life on a young planet: the first 3 billion years of evolution on earth*. Princeton, NJ: Princeton University Press.
2. Butterfield NJ. 2015 Early evolution of the Eukaryota. *Palaeontology* **58**, 5–17. (doi:10.1111/pala.12139)
3. Butterfield NJ. 2015 Proterozoic photosynthesis—a critical review. *Palaeontology* **58**, 953–972. (doi:10.1111/pala.12211)
4. Cohen PA, Macdonald FA. 2015 The Proterozoic record of eukaryotes. *Paleobiology* **41**, 610–632. (doi:10.1017/pab.2015.25)
5. Knoll AH. 2014 Paleobiological perspectives on early eukaryotic evolution. *Cold Spring Harb. Perspect. Biol.* **6**, a016121. (doi:10.1101/cshperspect.a016121)
6. Muscente AD *et al*. 2017 Exceptionally preserved fossil assemblages through geologic time and space. *Gondwana Res.* **48**, 164–188. (doi:10.1016/j.gr.2017.04.020)
7. Butterfield NJ. 1995 Secular distribution of Burgess-Shale-type preservation. *Lethaia* **28**, 1–13. (doi:10.1111/j.1502-3931.1995.tb01587.x)
8. Gaines RR. 2014 Burgess Shale-type preservation and its distribution in space and time. *Paleontol. Soc. Pap.* **20**, 123–146. (doi:10.1017/S1089332600002837)
9. Anderson RP, Tosca NJ, Gaines RR, Mongiardino Koch N, Briggs DEG. 2018 A mineralogical signature for Burgess Shale-type fossilization. *Geology* **46**, 347–350. (doi:10.1130/G39941.1)
10. Saleh F, Pittet B, Perrillat J-P, Lefebvre B. 2019 Orbital control on exceptional fossil preservation. *Geology* **47**, 103–106. (doi:10.1130/G45598.1)
11. McMahon S, Anderson RP, Saupe EE, Briggs DEG. 2016 Experimental evidence that clay inhibits bacterial decomposers: implications for preservation of organic fossils. *Geology* **44**, 867–870. (doi:10.1130/G38454.1)
12. Naimark E, Kalinina M, Shokurov A, Boeva N, Markov A, Zaytseva L. 2016 Decaying in different clays: implications for soft-tissue preservation. *Palaeontology* **59**, 583–595. (doi:10.1111/pala.12246)
13. Naimark EB, Kalinina MA, Shokurov AV, Markov AV, Boeva NM. 2016 Decaying of *Artemia salina* in clay colloids: 14-month experimental formation of subfossils. *J. Paleontol.* **90**, 472–484. (doi:10.1017/jpa.2016.23)
14. Wilson LA, Butterfield NJ. 2014 Sediment effects on the preservation of Burgess Shale-type compression fossils. *Palaios* **29**, 145–154. (doi:10.2110/palo.2013.075)
15. Martin D, Briggs DEG, Parkes RJ. 2003 Experimental mineralization of invertebrate eggs and the preservation of Neoproterozoic embryos. *Geology* **31**, 39–42. (doi:10.1130/0091-7613(2003)031<0039:EMOIEA>2.0.CO;2)
16. Naimark E, Kalinina M, Boeva N. 2018 Persistence of external anatomy of small crustaceans in a long term taphonomic experiment. *Palaios* **33**, 154–163. (doi:10.2110/palo.2017.083)
17. Naimark E, Kalinina M, Shokurov A, Markov A, Zaytseva L, Boeva N. 2018 Mineral composition of host sediments influences the fossilization of soft tissues. *Can. J. Earth Sci.* **55**, 1271–1283. (doi:10.1139/cjes-2017-0237)
18. Newman S, Daye M, Fakra SC, Marcus MA, Pajusalu M, Pruss SB, Smith EF, Bosak T. 2019 Experimental preservation of muscle tissue in quartz sand and kaolinite. *Palaios* **34**, 437–451. (doi:10.2110/palo.2019.030)
19. Orr PJ, Briggs DEG, Kearns SL. 1998 Cambrian Burgess Shale animals replicated in clay minerals. *Science* **281**, 1173–1175. (doi:10.1126/science.281.5380.1173)
20. Anderson RP. 2019 Clay minerals and the fossilisation of early complex life. In *The origin and rise of complex life: integrating models, geochemical and palaeontological data* (eds R Wood, AG Liu, TM Lenton, SW Poulton, PCJ Donoghue). London, UK: The Royal Society.
21. Anderson EP, Schiffbauer JD, Xiao SH. 2011 Taphonomic study of Ediacaran organic-walled fossils confirms the importance of clay minerals and pyrite in Burgess Shale-type preservation. *Geology* **39**, 643–646. (doi:10.1130/G31969.1)
22. Wacey D *et al*. 2016 Contrasting microfossil preservation and lake chemistries within the 1200–1000 Ma Torridonian Supergroup of NW Scoland. In *Earth system evolution and early life: a celebration of the work of Martin Brasier* (eds AT Brasier, D McIlroy, N McLoughlin). London, UK: The Geological Society.
23. Wacey D, Saunders M, Roberts M, Menon S, Green L, Kong C, Culwick T, Strother P, Brasier MD. 2014 Enhanced cellular preservation by clay minerals in 1 billion-year-old lakes. *Sci. Rep.* **4**, 5841. (doi:10.1038/srep05841)
24. Hermann TN, Podkovyrov VN. 2010 A discovery of Riphean heterotrophs in the Lakhanda Group of Siberia. *Paleontol. J.* **44**, 374–383.
25. Hermann TN. 1990 *Organic world one billion years ago*. Leningrad, Russia: Nauka.
26. Butterfield NJ, Knoll AH, Swett K. 1994 Paleobiology of the Neoproterozoic Svanbergfjellet Formation, Spitsbergen. *Foss. Strata* **34**, 1–84. (doi:10.1111/j.1502-3931.1994.tb01558.x)
27. Tang Q, Pang K, Yuan X, Xiao S. 2020 A one-billion-year-old multicellular chlorophyte. *Nat. Ecol. Evol.* **4**, 543–549. (doi:10.1038/s41559-020-1122-9)

28. Butterfield NJ. 2005 Probable Proterozoic fungi. *Paleobiology* **31**, 165–182. (doi:10.1666/0094-8373(2005)031<0165:PPF>2.0.CO;2)
29. Butterfield NJ, Rainbird RH. 1998 Diverse organic-walled fossils, including 'possible dinoflagellates,' from the early Neoproterozoic of arctic Canada. *Geology* **26**, 963–966. (doi:10.1130/0091-7613(1998)026<0963:DOWFIP>2.3.CO;2)
30. Briggs DEG, Summons RE. 2014 Ancient biomolecules: their origins, fossilization, and role in revealing the history of life. *BioEssays* **36**, 482–490. (doi:10.1002/bies.201400010)
31. Tegelaar EW, de Leeuw JW, Derenne S, Largeau C. 1989 A reappraisal of kerogen formation. *Geochim. Cosmochim. Acta* **53**, 3103–3106. (doi:10.1016/0016-7037(89)90191-9)
32. Hoiczyk E. 1998 Structural and biochemical analysis of the sheath of *Phormidium uncinatum*. *J. Bacteriol.* **180**, 3923–3932. (doi:10.1128/JB.180.15.3923-3932.1998)
33. Walsh K, Jones GJ, Dunstan RH. 1997 Effect of irradiance on fatty acid, carotenoid, total protein composition and growth of *Microcystis aeruginosa*. *Photochemistry* **44**, 817–824. (doi:10.1016/S0031-9422(96)00573-0)
34. Bernard S, Benzerara K, Beyssac O, Balan E, Brown Jr GE. 2015 Evolution of the macromolecular structure of sporopollenin during thermal degradation. *Heliyon* **1**, e00034. (doi:10.1016/j.heliyon.2015.e00034)
35. Snyder RL, Bish DL. 1989 Quantitative analysis. *Rev. Mineral. Geochem.* **20**, 101–144.
36. Środoń J, Drits VA, McCarty DK, Hsieh JCC, Eberl DD. 2001 Quantitative X-ray diffraction analysis of clay-bearing rocks from random preparations. *Clays Clay Miner.* **49**, 514–528. (doi:10.1346/CCMN.2001.0490604)
37. Russell JD, Fraser AR. 1994 Infrared methods. In *Clay mineralogy: spectroscopic and chemical determinative methods* (ed. MJ Wilson), pp. 11–67. London, UK: Champman and Hall.
38. Thomson D, Rainbird RH, Dix G. 2014 Architecture of a Neoproterozoic intracratonic carbonate ramp succession: Wynniatt Formation, Amundsen Basin, Arctic Canada. *Sediment. Geol.* **299**, 119–138. (doi:10.1016/j.sedgeo.2013.11.005)
39. Wilson MJ. 2013 *Rock forming minerals, 3C: clay minerals*. London, UK: The Geological Society.
40. Marshall CP, Javaux EJ, Knoll AH, Walter MR. 2005 Combined micro-Fourier transform infrared (FTIR) spectroscopy and micro-Raman spectroscopy of Proterozoic acritarchs: a new approach to Palaeobiology. *Precambrian Res.* **138**, 208–224. (doi:10.1016/j.precamres.2005.05.006)
41. Podkovyrov VN. 2009 Mesoproterozoic Lakhanda Lagerstätte, Siberia: Paleoecology and taphonomy of the microbiota. *Precambrian Res.* **173**, 146–153. (doi:10.1016/j.precamres.2009.04.006)
42. Powell W. 2003 Greenschist-facies metamorphism of the Burgess Shale and its implications for models of fossil formation and preservation. *Can. J. Earth Sci.* **40**, 13–25. (doi:10.1139/e02-103)
43. Briggs DEG, Kear AJ. 1993 Fossilization of soft tissue in the laboratory. *Science* **259**, 1439–1442. (doi:10.1126/science.259.5100.1439)
44. Skujinš, J, Pukite A, McLaren AD. 1974 Adsorption and activity of chitinase on kaolinite. *Soil Biol. Biochem.* **6**, 179–182. (doi:10.1016/00380717(74)90024-8)
45. Theng BKG. 1974 *The chemistry of clay-organic reactions*. New York, NY: John Wiley & Sons.
46. Yu WH, Li N, Tong DS, Zhou CH, Lin CX, Xu CY. 2013 Adsorption of proteins and nucleic acids on clay minerals and their interactions: a review. *Appl. Clay Sci.* **80–81**, 443–452. (doi:10.1016/j.clay.2013.06.003)
47. Sposito G. 1984 *The surface chemistry of soils*. Oxford, UK: Oxford University Press.
48. Liu X, Lu X, Sprik M, Cheng J, Meijer EJ, Wang R. 2013 Acidity of edge surface sites of montmorillonite and kaolinite. *Geochim. Cosmochim. Acta* **117**, 180–190. (doi:10.1016/j.gca.2013.04.008)
49. Solomon DH, Rosser MJ. 1965 Reactions catalyzed by minerals. Part 1. Polymerization of styrene. *J. App. Polym. Sci.* **9**, 1261–1271. (doi:10.1002/app/1965.070090407)
50. Pan C, Geng A, Zhong N, Liu J. 2010 Kerogen pyrolysis in the presence and absence of water and minerals: steranes and triterpenoids. *Fuel* **89**, 336–345. (doi:10.1016/j.fuel.2009.06.032)
51. Stimler NP, Tanzer ML. 1977 Location of the intermolecular cross linking sites in collagen. In *Protein crosslinking* (ed. M Friedman), pp. 675–697. Boston, MA: Springer.
52. Saleh F, Antcliffe JB, Lefebvre B, Pittet B, Laibl L, Perez F, Lustri L, Gueriau P, Daley AC. 2020 Taphonomic bias in exceptionally preserved biotas. *Earth Planet. Sci. Lett.* **529**, 115873. (doi:10.1016/j.epsl.2019.115873)
53. Konhauser KO, Fisher QJ, Fyfe WS, Longstaffe FJ, Powell MA. 1998 Authigenic mineralization and detrital clay binding by freshwater biofilms: the Brahmani River, India. *Geomicrobiol. J.* **15**, 209–222. (doi:10.1080/01490459809378077)
54. Konhauser KO, Fyfe WS, Ferris FG, Beveridge TJ. 1993 Metal sorption and mineral precipitation by bacteria in two Amazonian river systems: Rio Solimoes and Rio Negro, Brazil. *Geology* **161**, 399–413.
55. Konhauser KO, Urrutia MO. 1999 Bacterial clay authigenesis: a common biogeochemical process. *Chem. Geol.* **161**, 399–413. (doi:10.1016/S0009-2541(99)00118-7)
56. Ferris FG, Fyfe WS, Beveridge TJ. 1988 Metallic ion binding by *Bacillus subtilis*: implications for the fossilization of microorganisms. *Geology* **16**, 149–152. (doi:10.1130/0091-7613(1988)016<0149:MIBBBS>2.3.CO;2)
57. Newman SA, Klepac-Ceraj V, Mariotti G, Pruss SB, Watson N, Bosak T. 2017 Experimental fossilization of mat-forming cyanobacteria in coarse-grained siliciclastic sediments. *Geobiology* **15**, 484–498. (doi:10.1111/gbi.12229)
58. Newman SA, Mariotti G, Pruss SB, Bosak T. 2016 Insights into cyanobacterial fossilization in Ediacaran siliciclastic environments. *Geology* **44**, 579–582. (doi:10.1130/G37791.1)
59. Knoll AH. 1985 Exceptional preservation of photosynthetic organisms in silicified carbonates and silicified peats. *Phil. Trans. R. Soc. Lond. B* **311**, 111–122. (doi:10.1098/rstb.1985.0143)
60. Li Z-X, Evans DAD, Halverson GP. 2013 Neoproterozoic glaciations in a revised global palaeogeography from the breakup of Rodinia to the assembly of Gondwanaland. *Sediment. Geol.* **294**, 219–232. (doi:10.1016/j.sedgeo.2013.05.016)
61. Halevy I, Bachan A. 2017 The geologic history of seawater pH. *Science* **355**, 1069–1071. (doi:10.1126/science.aal4151)
62. dos Reis M, Thawornwattana Y, Angelis K, Telford MJ, Donoghue PCJ, Yang Z. 2015 Uncertainty in the timing of origin of animals and the limits of precision in molecular timescales. *Curr. Biol.* **25**, 2939–2950. (doi:10.1016/j.cub.2015.09.066)
63. Bobrovskiy I, Hope JM, Ivantsov A, Nettersheim BJ, Hallmann C, Brocks JJ. 2018 Ancient steroids establish the Ediacaran fossil *Dickinsonia* as one of the earliest animals. *Science* **361**, 1246–1249. (doi:10.1126/science.aat7228)
64. Runnegar B. 1982 The Cambrian explosion: animals or fossils? *J. Geol. Soc. Aust.* **29**, 395–411. (doi:10.1080/00167618208729222)
65. Betts HC, Puttick MN, Clark JW, Williams TA, Donoghue PCJ, Pisani D. 2018 Integrated genomic and fossil evidence illuminates life's early evolution and eukaryote origin. *Nature Ecology and Evolution* **2**, 1556–1562. (doi:10.1038/s41559-018-0644-x)
66. Briggs DEG, Erwin DH, Collier FJ. 1994 *Fossils of the Burgess Shale*. Washington, DC: Smithsonian Institution Press.
67. Hou X, Siveter DJ, Siveter DJ, Aldridge RJ, Cong P, Gabbott SE, Ma X, Purnell MA, Williams M. 2017 *The Cambrian fossils of Chengjiang, China: the flowering of early animal life*, 2nd edn. Oxford, UK: John Wiley & Sons Ltd.
68. Butterfield NJ, Harvey THP. 2012 Small carbonaceous fossils (SCFs): a new measure of early Paleozoic paleobiology. *Geology* **40**, 71–74. (doi:10.1130/g32580.1)
69. Harvey THP, Butterfield NJ. 2017 Exceptionally preserved Cambrian loriciferans and the early animal invasion of the meiobenthos. *Nat. Ecol. Evol.* **1**, 0022. (doi:10.1038/s41559-016-0022)
70. Butterfield NJ. 2004 A vaucheriacean alga from the middle Neoproterozoic of Spitsbergen: implication for the evolution of Proterozoic eukaryotes and the Cambrian explosion. *Paleobiology* **30**, 231–252. (doi:10.1666/0094-8373(2004)030<0231:AVAFTM>2.0.CO;2)
71. Butterfield NJ. 2009 Modes of pre-Ediacaran multicellularity. *Precambrian Res.* **173**, 201–211. (doi:10.1016/j.precamres.2009.01.008)
72. Cohen PA, Knoll AH, Kodner RB. 2009 Large spinose microfossils in Ediacaran rocks as resting stages of early animals. *Proc. Natl Acad. Sci. USA* **106**, 6519–6524. (doi:10.1073/pnas.0902322106)

73. Cornet Y, François C, Compère P, Callec Y, Roberty S, Plumier JC, Javaux EJ. 2019 New insights on the paleobiology, biostratigraphy, and paleogeography of the pre-Sturtian microfossil index taxon *Cerebrosphaera*. *Precambrian Res.* **322**, 105410. (doi:10.1016/j.precamres.2019.105410)
74. Shang X, Liu P, Moczydłowksa M. 2019 Acritarchs from the Doushantuo Formation at Liujing section in Songlin area of Guizhou Province, South China: implications for early-middle Ediacaran biostratigraphy. *Precambrian Res.* **334**, 105453. (doi:10.1016/j.precamres.2019.105453)
75. Tang Q, Pang T, Yuan X, Xiao S. 2017 Electron microscopy reveals evidence for simple multicellularity in the Proterozoic fossil *Chuaria*. *Geology* **45**, 75–78. (doi:10.1130/G38680.1)
76. McMahon S, Bosak T, Grotzinger JP, Milliken RE, Summons RE, Newman S, Fraeman A, Williford KH, Briggs DEG. 2018 A field guide to finding fossils on Mars. *J. Geophys. Res. Planets* **123**, 1012–1040. (doi:10.1029/2017JE005478)
77. Ehlmann BL, Mustard JF, Murchie SL, Bibring J-P, Meunier A, Fraeman AA, Langevin Y. 2011 Subsurface water and clay mineral formation during the early history of Mars. *Nature* **479**, 53–60. (doi:10.1038/nature10582)
78. Ehlmann BL *et al*. 2009 Identification of hydrated silicate minerals on Mars using MRO-CRISM: geologic context near Nili Fossae and implications for aqueous alteration. *J. Geophys. Res. Planets* **114**, E00D08. (doi:10.1029/2009JE003339)
79. Cino CD, Dehouck E, McLennan SM. 2017 Geochemical constraints on the presence of clay minerals in the Burns formation, Meridiani Planum, Mars. *Icarus* **281**, 137–150. (doi:10.1016/j.icarus.2016.08.029)
80. Cuadros J. 2015 Clays are messy—also on Mars. *Am. Mineral.* **100**, 669–670. (doi:10.2138/am-2015-5229)
81. Xiao S, Yuan X, Steiner M, Knoll AH. 2002 Macroscopic carbonaceous compressions in a terminal Proterozoic shale: a systematic reassessment of the Miaohe biota, South China. *J. Paleontol.* **76**, 347–376. (doi:10.1017/S0022336000041743)